Stanford Exploration Project, Report 73, November 18, 1997, pages 257–284

On the imaging condition for elastic reverse-time migration

Carlos A. Cunha Filho[1]

keywords: *imaging, modeling, reflectivity, velocity, elastic, estimation, correlation*

ABSTRACT

Migration-based methods have been proposed recently as a solution for correctly estimating angle-dependent reflectivity in the presence of complex structures. I evaluate the use of different imaging conditions for anisotropic prestack reverse-time migration that aim the estimation of the reflectivity as a function of the local illumination angle. Emphasis is given to a particular imaging criterion that generates four simultaneous images. These images correspond to the in-depth (local) plane-wave response for P–P, P–S, S–P, and S–S modes and can be used in a Zoeppritz-based elastic inversion scheme.

INTRODUCTION

Initial methods for recovering the angle-dependent reflectivity function were based on the assumption that the subsurface layers are nearly horizontal within the range covered by a common midpoint (CMP) gather which is the basic assumption of standard CMP processing (Newman, 1973; Yu, 1985; Kolb and Chapel, 1989; Cunha, 1990). Although these methods properly compensate for the long wavelength losses in a reasonable number of practical problems, they cannot be applied to areas with structurally complex geology.

Recently, some more powerful methods for estimating the angle-dependent reflectivity, based on migration algorithms, have been developed. De Bruin et al. (1990a) presented a method for estimating the angle-dependent reflectivity using a scalar pre-stack $x-\omega$ migration scheme. First, the multi-component data were decomposed into P–P, P–S, S–P and S–S modes and each of them migrated separately. Tests with synthetic data showed that the method was able to retrieve the reflectivity function with considerable accuracy for horizontal layers, but when dip was present (de Bruin, 1990b), the retrieved function was incorrectly shifted (in angle) because of the assumption of a horizontally-layered earth which is implicit in their imaging principle (integration along constant Snell parameter traces). Another limitation in their

[1]**email:** not available

method is that the estimated reflectivities do not correspond to the local, in depth, reflectivities because the decomposition is carried out before the depth extrapolation. As a result, a wavefield that leaves and arrives at the surface as a pure compressional mode (marine data) but is associated to a S–S reflection (PSSP mode) will not be imaged by their method. Lumley and Beydoun (1991) introduced a different method for retrieving the reflectivity function, using an elastic pre-stack Kirchhoff migration scheme. Their imaging principle was not limited by the horizontal layer assumption and was successfully applied to synthetic and real data. As a consequence of the Kirchhoff approach, their method suffers the restrictions imposed by the ray approximation associated with the evaluation of the Green's function. Both methods, however, assume that the medium is isotropic and attempt to image only the converted modes associated with a single conversion at the reflection plane. Therefore, when applied to off-shore data, only PP reflectivities can be obtained with these approaches.

This paper discusses the imaging condition for retrieving the angle-dependent reflectivity using anisotropic prestack reverse time migration (RTM). With two different approaches to the imaging condition, Mora (1986), and Chang and McMechan (1987) introduced an elastic isotropic formulation for RTM. Etgen (1987) extended the extrapolation step for the general anisotropic case, but was able to migrate only S_H modes because of the restriction imposed by the scalar formulation of the imaging condition. Karrenbach (1991) developed an anisotropic reverse-time migration/inversion scheme using a tensorial imaging condition represented by the crosscorrelation between the different components of the upcoming and downgoing wavefields. Each of the resulting images is associated with a perturbation in one component of the stiffness tensor. His approach is equivalent to the first step of a linearized inverse algorithm because it backward propagates the residuals between the forward modeled and the recorded wavefields at the receivers, rather than just the recorded wavefield. As a result, the images were more closely related to perturbations in the impedance, instead of to the reflectivity functions.

The imaging conditions and imaging criteria discussed here are implemented in a reverse-time migration method described in Cunha (1992). The final result of the migration corresponds to four images, which are associated with the angle-dependent reflectivity functions for P–P, P–S, S–P, and S–S modes.

IMAGING PRINCIPLE

Migration includes two distinct steps: downward extrapolation in depth or backward extrapolation in time, and imaging for the desired attribute. When the desired attribute is related to the impedance contrasts in the subsurface Claerbout's imaging principle (Claerbout, 1971) represents the basis for many imaging condition equations. According to this principle, a reflector exists at a point where the upcoming and the downgoing wavefields coincide in time and space. There are two distinct aspects behind this principle: the choice of the specific attribute that we seek to image (*imaging condition*), and the definition of the procedure to be used in the estimation of that attribute (*imaging criterion*).

If the migration is designed with the sole purpose of obtaining a structural image of the compressional impedance contrasts in the subsurface, then the image condition must be formulated so that it favors noise reduction over amplitude preservation. If however the goal is to obtain an image of attributes that can be correlated to the fluid content of porous rocks, or used as the basic information for a lithological inversion scheme, then the imaging condition must represent a statistically meaningful estimation of that attribute.

IMAGING CONDITION

This section considers the definition of "instantaneous" imaging conditions without addressing the problems of how to deal with stabilization requirements when the amplitude of the incident field is small, or how to do the time average to obtain a meaningful estimation.

P–P reflection coefficient

In most practical cases only purely compressional modes can be resolved from conventional surface seismic, especially if the data were collected in a marine environment where shear waves cannot be generated or recorded. In such cases the only reliable reflection coefficient to image is the one associated to P to P reflection.

Reflection coefficients are often defined for either displacement-amplitude ratios or potential ratios. For a pure compressional wave the displacement field can be expressed as the gradient of a potential field. Taking the divergence of the displacement and using the wave-equation for the potential leads to

$$\phi(x,z,\omega) \;=\; \frac{v_p^2}{\omega^2}\,\nabla^2\phi(x,z,\omega) \;=\; \frac{v_p^2}{\omega^2}\,\nabla\cdot\mathbf{u}(x,z,\omega). \tag{1}$$

It is clear that the above formulation is restricted to isotropic cases where P waves are described by a single velocity v_p, however the background media, used for the time extrapolation is considered to be anisotropic. This means that anisotropic behavior is correctly handled in the propagation through the overburden, but not at the target zone. The displacement reflection coefficient relates to the potential reflection coefficient through

$$\text{Displacement coefficient} \;=\; \frac{v_{inc}}{v_{ref}}\;\text{Potential coefficient},$$

Aki and Richards (1980). Since the velocities for the incident and reflected wave, are the same, the imaging condition for obtaining the P–P displacement reflection coefficient can be formulated as

$$R_{PP}(x,z,t) \;=\; \frac{\phi^r(x,z,t)}{\phi^s(x,z,t)} \;=\; \frac{\nabla \cdot \mathbf{u^r}(x,z,t)}{\nabla \cdot \mathbf{u^s}(x,z,t),} \tag{2}$$

where superscripts r and s correspond, respectively, to the reverse propagated *recorded* wavefield and to the forward propagated *shot* wavefield.

It is important to emphasize that the wavefield decomposition to separate the purely compressional field is performed only at the imaging step but the propagation (depth extrapolation) uses the full wavefield. Therefore, all elastic effects of mode conversion in all interfaces are taken into account.

P–S and S–P reflection coefficients

Similarly, a pure S_v shear mode can be described by the curl of a vector potential. To isolate the shear wave it is enough to apply a curl operator to the displacement field.

$$\boldsymbol{\chi}(x,z,\omega) \;=\; \nabla \times \mathbf{u}(x,z,\omega) \;=\; \nabla \times \nabla \times \boldsymbol{\psi}(x,z,\omega), \tag{3}$$

For this 2-D implementation the wavefields are invariant in the direction of the unit vector normal to the experiment plane ($\hat{\mathbf{y}}$). As a result, the only non vanishing component of $\boldsymbol{\chi}$ will be in the $\hat{\mathbf{y}}$ direction. Defining

$$\chi(x,z,\omega) \;=\; (\nabla \times \mathbf{u}(x,z,\omega)) \cdot \hat{\mathbf{y}},$$

and using the same approach used for P–P, results in the following equation to describe the imaging condition for the P–S reflection coefficient

$$R_{PS}(x,z,t) \;=\; \frac{v_p \; \chi^r(x,z,t)}{v_s \; \phi^s(x,z,t)} \;=\; \frac{v_s \; (\nabla \times \mathbf{u^r}(x,z,t)) \cdot \hat{\mathbf{y}}}{v_p \; \nabla \cdot \mathbf{u^s}(x,z,t)}, \tag{4}$$

and for the S–P reflection coefficient

$$R_{SP}(x,z,t) \;=\; \frac{v_s \; \phi^r(x,z,t)}{v_p \; \chi^s(x,z,t)} \;=\; \frac{v_p \; \nabla \cdot \mathbf{u^r}(x,z,t)}{v_s \; (\nabla \times \mathbf{u^s}(x,z,t)) \cdot \hat{\mathbf{y}}} \tag{5}$$

S–S reflection coefficient

The treatment here is analogous to the one for the P–S and S–P coefficients. The final relation is:

$$R_{SS}(x,z,t) \;=\; \frac{\chi^r(x,z,t)}{\chi^s(x,z,t)} \;=\; \frac{(\nabla \times \mathbf{u^r}(x,z,t)) \cdot \hat{\mathbf{y}}}{(\nabla \times \mathbf{u^s}(x,z,t)) \cdot \hat{\mathbf{y}}} \tag{6}$$

Scattering matrix coefficient

For anisotropic media, it is necessary to make the distinction between group and phase properties. The equations relating the several reflection and transmission coefficients with the elastic properties of the medium are derived for plane waves, which imply that the coefficients are associated to ratios between *phase amplitudes*.

One possible approach is to perform a local plane-wave decomposition, integrating the component of the vector-wavefield in the local polarization direction ($\mathbf{j}(x,z,t)$) along different directions p in order to build a function $A(p,x,z,t)$, which represents the phase amplitude for each point of the space-time as a function of the horizontal slowness, and a polarization vector function $\mathbf{j}(x,z,t)$. Time averaging should in this case provide three expectations:$\tilde{A}(x,z)$, $\tilde{p}(x,z)$, and $\tilde{j}(x,z)$. Next we need to use the Christoffel equation with the background elastic parameters used in the migration to find the wave type associated with each polarization vector. Then, an anisotropic inversion scheme can estimate the elastic parameters that best fit the scattering relation involving $\tilde{A}$ for the different modes and $\mathbf{j}$, as a function of the horizontal slowness $\tilde{p}$.

Stiffnesses perturbations

Most imaging methods described in the literature involve the correlation between scalar wavefields. An exception is the tensorial imaging condition formulated by Karrenbach (1991):

$$\delta c_{jklm}(x,z,t) = \partial_m[\phi_l^s(x,z,t)]\partial_k[\delta\phi_j^r(x,z,t)],$$

where ϕ_l^s is the l component of the forward modeled shot wavefield, and $\delta\phi_j^r$ is the reverse propagated difference between the forward modeled wavefield at the receivers and the recorded wavefield. This process is equivalent to one step of a wavefield inversion scheme, and δc_{jklm} can be interpreted as the estimated perturbation in the stiffness tensor. In this sense, it can be considered as an extension of Tarantola's (1986) elastic inversion theory to the general anisotropic case.

Hildebrand (1987) used a variation of this principle to image for the acoustic impedance rather than the reflection coefficient, using reverse-time migration to extrapolate the pressure and particle-velocity wavefields. Contrary to the above formulation, Hildebrand's approach obtained a image of the impedance (rather than perturbations), using a recursive depth extrapolation procedure.

DEFINING AN IMAGING CRITERION

The imaging conditions discussed in the previous section obtain an estimation of the imaging attribute at a particular point in the four-dimensional (for a 2D treatment)

2D–space×time×shot-position domain. The imaging criterion defines the statistical approach involved to reduce these information to the expectation value of the attribute in the three-dimensional domain spanned by 2D–space×incidence-angle. There are two major paths to perform this reduction

$$data(x_r,t;x_s) \begin{array}{l} \xrightarrow{A} \; R(x,z,t;x_s) \; \xrightarrow{B} \; R(x,z;x_s) \\ \xrightarrow{A} \; \beta(x,z,t;x_s) \; \xrightarrow{B} \; \beta(x,z;x_s) \end{array} \xrightarrow{C} R(x,z,\beta), \tag{7}$$

or

$$data(x_r,t;x_s) \xrightarrow{A} R(x,z,\beta,t;x_s) \xrightarrow{B} R(x,z,\beta;x_s) \xrightarrow{C} R(x,z,\beta). \tag{8}$$

In the first path A represents the depth extrapolation and imaging for time t, B represents the time integration process and C represents the final search over different shot-gathers to build the function $R(x,z,\beta)$. In the second path A also represents the depth extrapolation and imaging for time t, B represents the time integration process and C represents the integration over the shot-point axis. The first one starts with an independent estimation of the attribute and the angle for each shotpoint, while the second obtains from the beginning an estimation of the angular distribution of the attribute for each shotpoint.

Correlation-based criterion

The usual approach to implement the imaging condition involves the zero-lag correlation between the reverse-propagated recorded wavefield and a function of the reverse-propagated modeled wavefield. The time correlation may also involve a weighting function (or a covariant operator) and a normalization factor. The general form is

$$R(x,z;x_s) \;=\; \frac{\int \, W(x,z,t;x_s)\; \phi^r(x,z,t;x_s)\; F[\phi^s(x,z,t;x_s)]\; dt}{\int \, W(x,z,t;x_s)\; dt}. \tag{9}$$

This criterion is obviously included in the category represented by (7), and implicitly requires the use of a smooth background velocity in the wavefield-extrapolation step. Ray-wavefield hybrid methods can be viewed as a particular case of (9), with $W = \delta(t-t_s)$, where $t_s = t_s(x,z;x_s)$ is the ray-theoretical traveltime.

Jacobs (1982) compared the implementation of three different forms of equation (9), in a pre-stack profile migration in the $\omega - x$ domain:

$$\begin{aligned} R_1 &= \int \phi^r \; [\phi^s]^* \; d\omega, \\ R_2 &= \int \phi^r \; \frac{[\phi^s]^*}{\mid \phi^s \mid} \; d\omega, \\ R_3 &= \int \phi^r \; \frac{[\phi^s]^*}{\mid \phi^s \mid^2 + \epsilon} \; d\omega. \end{aligned}$$

His conclusion was that R_3, though theoretically more correct for estimating the reflection coefficient, was too noise sensitive to be used in that migration scheme. There are two contradictory aspects between the imaging condition and the imaging criterion: while the former usually involves division by the modeled (incident) wavefield, the latter usually requires multiplication by the same wavefield to assure that only those estimations where the incident wavefield has significant energy will contribute effectively to the final expectation.

The implementation of the P–P reflectivity imaging-condition stated in equation 2 with the correlation criterion (9) uses the following definitions:

$$\begin{aligned} W(x,z,t;x_s) &= [\phi^s]^2(x,z,t;x_s), \\ E(x,z;x_s) &= \int W(x,z,t;x_s)\, dt \end{aligned}$$

and

$$F[\phi^s(x,z,t;x_s)] = \frac{1}{\phi^s(x,z,t;x_s)},$$

which results in

$$\begin{aligned} R(x,z;x_s) &= \frac{\int \phi^r(x,z,t;x_s)\phi^s(x,z,t;x_s)\, dt}{E(x,z;x_s)}, \quad \text{where } E(x,z;x_s) \geq E_{cut}(x,z;x_s), \\ R(x,z;x_s) &= \frac{\int \phi^r(x,z,t;x_s)\phi^s(x,z,t;x_s)\, dt}{E_{cut}(x,z;x_s)}, \quad \text{elsewhere}, \end{aligned} \tag{10}$$

and the local Snell parameter image as

$$\check{p}(x,z;x_s) = \frac{\int \mid \phi^r(x,z,t;x_s)\ \phi^s(x,z,t;x_s) \mid\ \tilde{p}(x,z,t;x_s)\, dt}{\int \mid \phi^r(x,z,t;x_s)\ \phi^s(x,z,t;x_s) \mid\ dt}, \tag{11}$$

where $\tilde{p}(x,z,t;x_s)$ is computed from the two wavefields ϕ^r and ϕ^s, as described in appendix A.

In the above equations, $E_{cut}(x,z;x_s)$ is a smooth function that should approximate a fraction of the inverse of the spherical divergence. Equation (10) gives the correct estimation of the reflection coefficient in the regions well illuminated by the source ($E(x,z;x_s) \geq E_{cut}(x,z;x_s)$) and a damped estimation in the dim regions.

Figures **??** and **??** show two images obtained with equations (10 and 11). The difference between these figures is that a smooth background model was used in the extrapolation step for Figure **??** and the original discontinuous model was used in the extrapolation step for Figure **??**. The source is located at position 800 meters and the receivers extends from 980 meters to 2480 meters.

Using a smooth background velocity avoids the contamination of the image by false reflectors originated by reflections in the extrapolation stage. In addition, the two wavefields involved in the migration correspond to unmixed modes (incident and reflected). One disadvantage is that transmission/conversion losses in the interfaces above the target are not compensated for in the extrapolation step. Another disadvantage is the loss in resolution caused by the higher dispersion in the wavefield extrapolation when a smooth background model is used[2].

[2]What I am comparing here is the total dispersion using a model with a few sharp transitions with the total dispersion using a similar model with smooth transitions (but same contrasts).

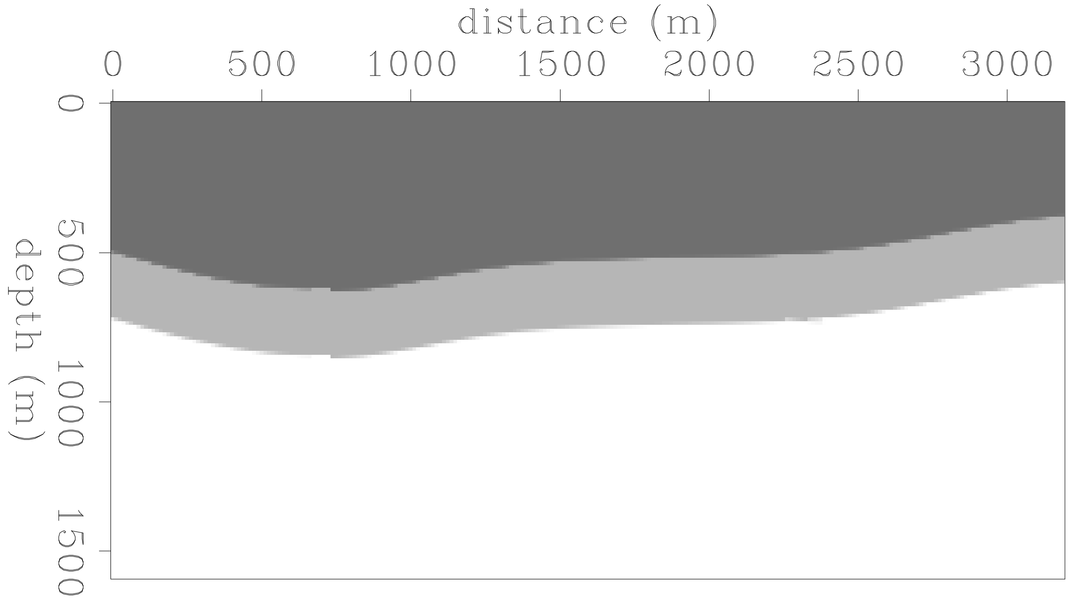

Figure 1: Elastic model used to generate the synthetic profiles that are used to illustrate the different imaging criteria. Only C_{11} is represented in the figure. The model is isotropic, that is, $C_{11} = C_{33}$ for all layers, and the first layer is water ($C_{55} = 0$). carlos3-model5 [ER]

When a non-smoothed background model is used in the extrapolation step the upward propagating modeled field and the downward propagating recorded field can be left out of the imaging computation, but the secondary reflections generated by them will generate false events in the final imaging. Also, at each interface (where the imaging computation is relevant) the two wavefields involved in the migration correspond to a superposition of several modes (incident, reflected, transmitted and converted) resulting in a contradictory application of the imaging principle. Nevertheless, there are two positive aspects in the use of a discontinuous model. First, the transmission/conversion losses are correctly compensated (at least for the incident wavefield ϕ^s.), and second, the small dispersion results in a superior resolution.

Figure **??** shows the images obtained for the other modes using the correlation criterion implementation of equations (4), (5), and (6). In this figure, both **??**-a and **??**-b refer to the PS reflectivity but while **??**-a was obtained using the true model, **??**-b was generated using a smoothed model for P velocities and discontinuous (true) for S velocities. The other two images, which correspond to SP (**??**-c) and SS (**??**-d) modes, were also obtained using the true velocity model. All the mode-converted images obtained with a smoothed velocity model were completely unreliable because the mode-conversion dynamics of smooth models is notably different from the mode-conversion dynamics of discontinuous media. Even when the discontinuous model is used we can see false events which are not related to the generation of multiples as in the PP case.

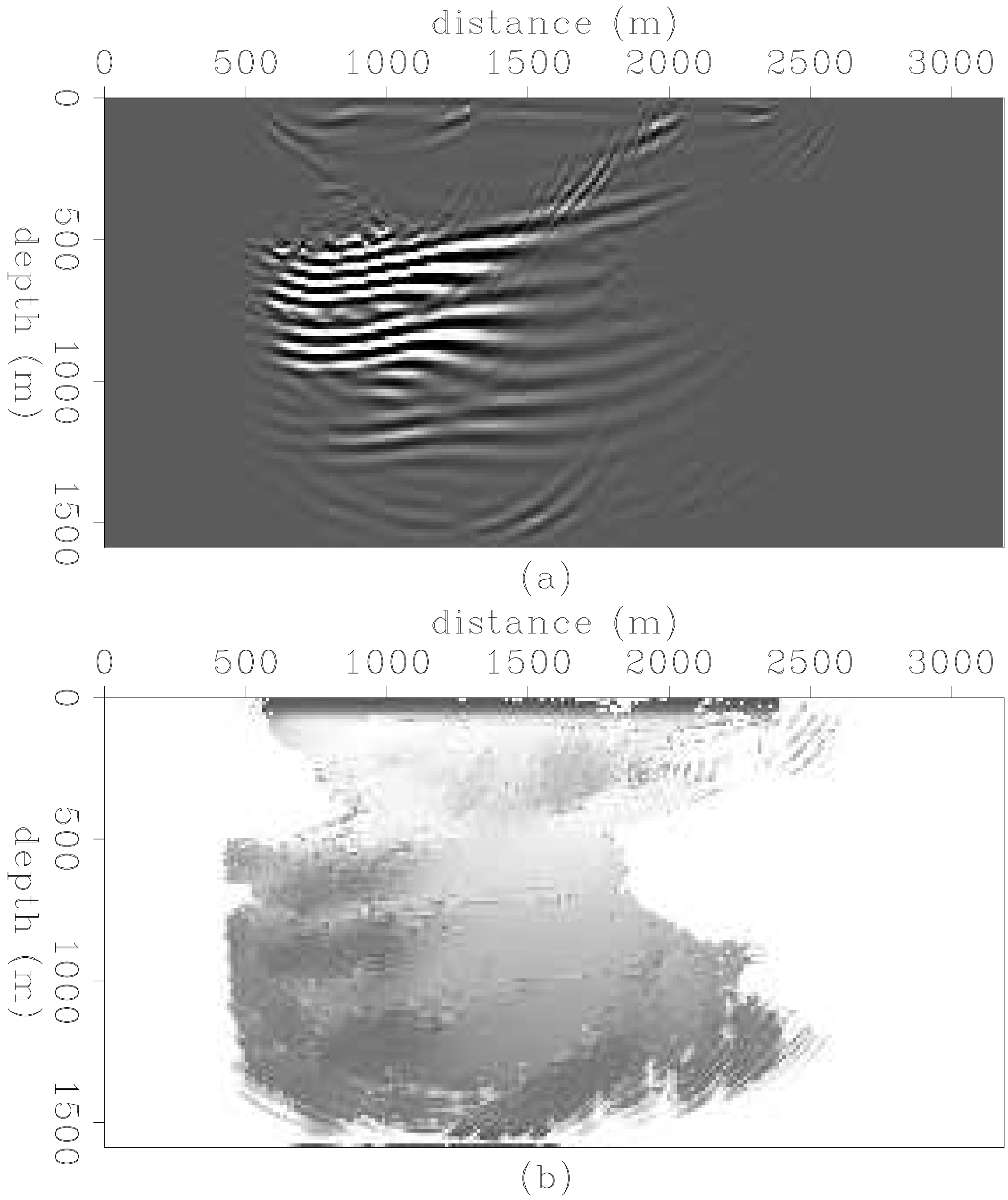

Figure 2: (a) Image of the P–P reflection coefficient for a single synthetic shot profile, using the correlation criterion and a smooth background model. (b) Imaging of the local Snell parameter associated with the reflection-coefficient-imaging in a. carlos3-migcorsmt [NR]

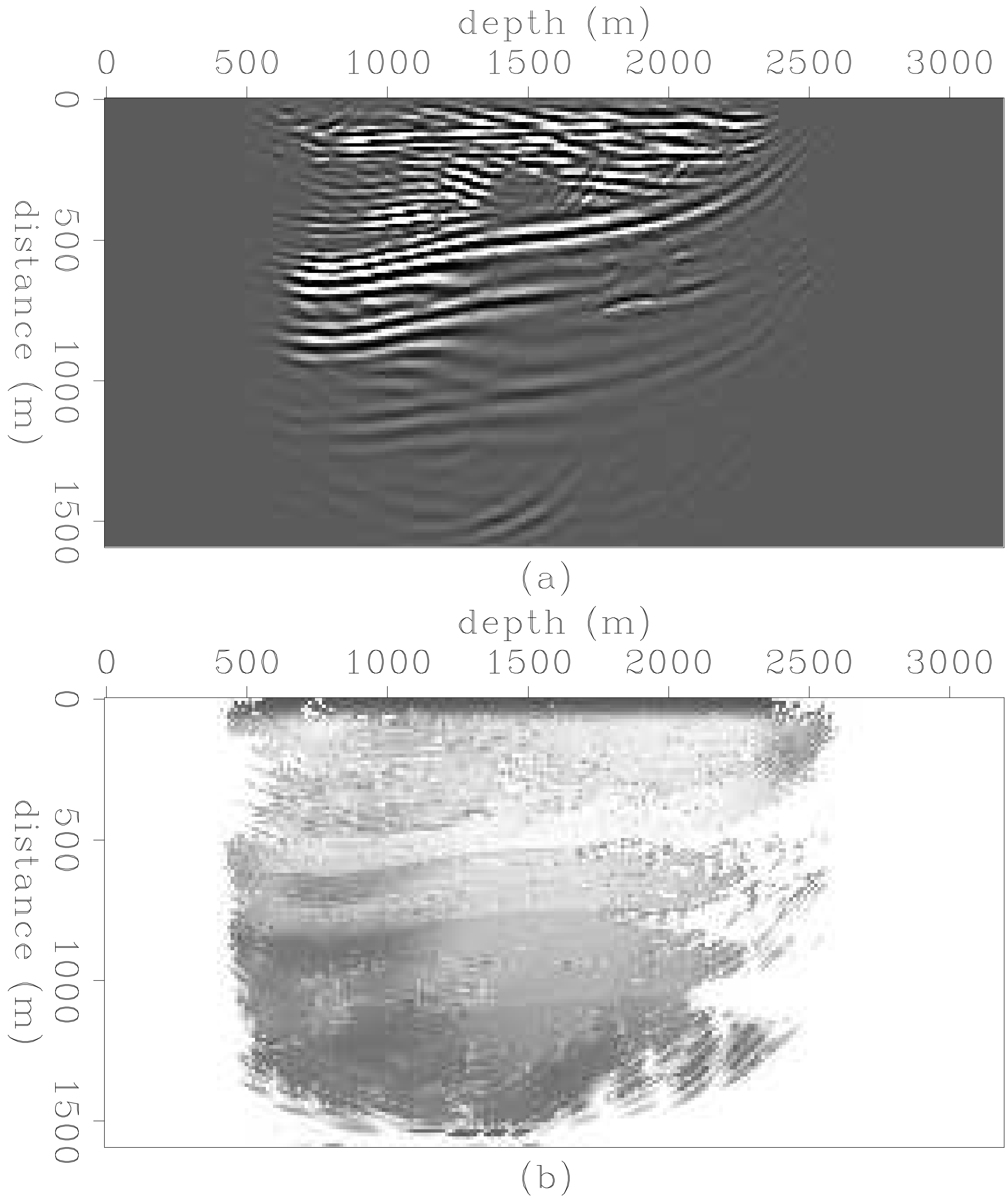

Figure 3: (a) Image of the P–P reflection coefficient for a single synthetic shot profile, using the correlation criterion and without smoothing the background model. (b) Imaging of the local Snell parameter associated with the reflection-coefficient-imaging in (a). carlos3-migcorblk [ER]

Although the ocean floor interface should be absent from all the converted-mode images we can see from the figure that it is actually present in all of them. The reason is that the reverse-propagating P wavefield is partially converted to S in the liquid-solid boundary and the correlation of this converted wavefield with the modeled wavefield (which is also also partially converted to S) produces the false images. These false images of the ocean floor are actually deeper than the PP images because they are formed below the boundary. There are however some positive aspects in these converted-mode images. As expected the regions where the propagation-direction of the wavefield is nearly normal to the interface are not imaged, while some strong reflections can be observed at regions where the incidence angle is large.

The V-stack criterion

It is possible to define an imaging criterion that does not produce undesirable false reflections when a discontinuous background model is used. Figure **??** shows the modeled wavefield and the reverse propagated recorded field at the same time. Not only the incident wavefield is reflected and transmitted (only the P wave component is shown) but also the backward-propagated recorded wavefield.

The difference is that, because of its limited aperture, the reflections originating from the reverse propagation of recorded wavefield will be limited to a small region of space. As illustrated in the same figure, the product of the two wavefields has a peculiar **V** shape with vertex at the reflector. Figure **??** illustrates this concept for a synthetic shot profile.

Application of this imaging criterion is not straightforward. The following steps can be used to implement the V-stack criterion:

- Define the product function Ψ^{rs}

$$\Psi^{rs}(x,z,t;x_s) \;=\; \phi^r(x,z,t;x_s)\;\phi^s(x,z,t;x_s)$$

- Calculate the local semblance of Ψ along all directions (θ) around every point (x,z) of the profile x_s

$$\mathrm{Semb}[\Psi(x,z,t,\theta;x_s)] = \frac{\left[\int_0^{\Delta l}\Psi^{rs}(x+l\cos\theta, z\;+l\sin\theta, t, x_s)\;dl\right]^2}{\int_0^{\Delta l}[\Psi^{rs}(x+l\cos\theta, z+l\sin\theta, t, x_s)]^2\;dl},$$

  where Δl is the size of the local stacking segment.

- Find the two directions θ_s and θ_r for which $\mathrm{Semb}[\Psi]$ is maximum.

- The estimation of the reflection coefficient is given by

$$R(x,z;x_s) = \frac{\int\,[\int_0^{\Delta l}\phi_r(x+l\cos\theta_r, z+l\sin\theta_r, t; x_s)\;dl\;\;\int_0^{\Delta l}\phi^s(x+l\cos\theta_s, z+l\sin\theta_s)\;dl]\;dt}{\int\,[\int_0^{\Delta l}\phi^s(x+l\cos\theta_s, z+l\sin\theta_s)\;dl]^2\;dt}$$

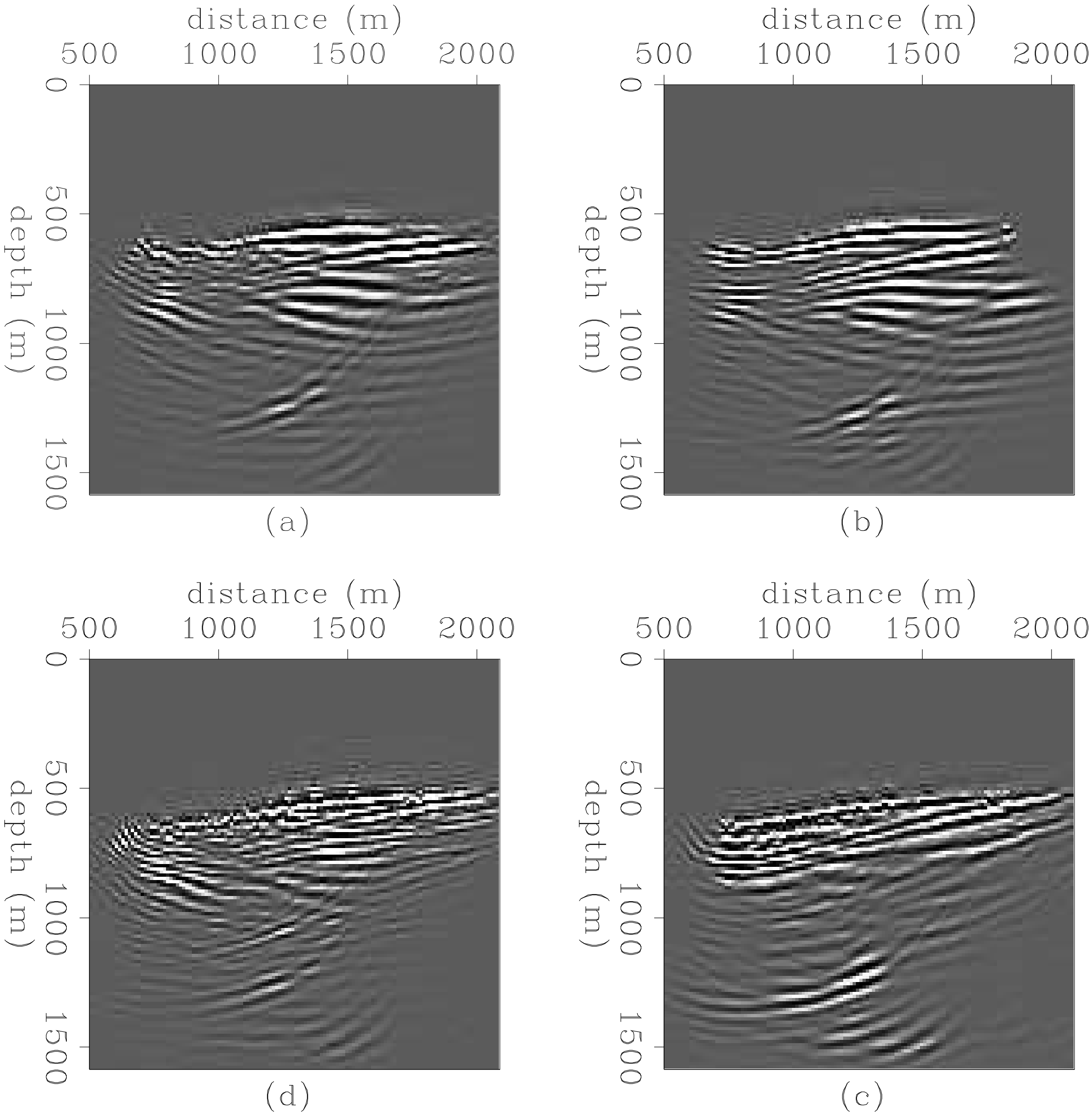

Figure 4: (a) Images of the P–S, S–P, and S–S reflection coefficients for the same synthetic gather of figure **??**. (a) P–S reflectivity using the unsmoothed velocity model. (b) P–S reflectivity using a smoothed P velocity and the unsmoothed S velocity. (c) S–P reflectivity using the unsmoothed velocity model. (d) S–S reflectivity using the unsmoothed velocity model. carlos3-mig4blk [NR]

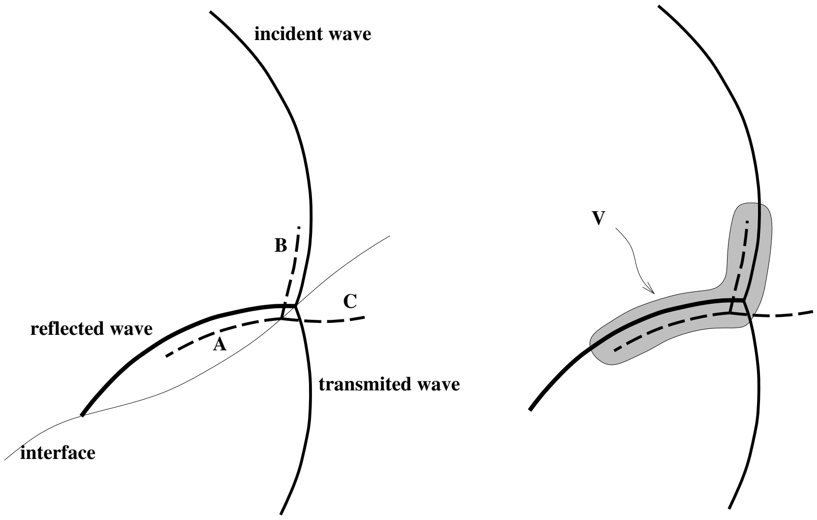

Figure 5: **Right:** The **continuous** thick line represents the modeled wavefield ϕ^s which is reflected and transmitted at the interface of a discontinuous background model. The **dashed** line represents the backward propagated recorded wavefield ϕ^r with an incident part **A**, which is also reflected **B** and transmitted **C** at the interface. **Left:** The overlapping region of both wavefields define a region with a characteristic "V" shape. carlos3-vstack [NR]

where $$\beta = \frac{\pi - \mid \theta_s - \theta_r \mid}{2}$$ is the angle of incidence.

This criterion offers two advantages for the case of non-smooth backgrounds relative to the correlation criterion. It will not have spurious events caused by the overlap of secondary reflections, and the attribute is estimated from wavefield contributions away from the interface, where the interference with other modes is much weaker. These same advantages are present in the next criterion.

Plane-wave decomposition criterion

The relevance of obtaining an estimation of the several angle-dependent reflection coefficients is the prospect of later using these information in a Zoeppritz-based elastic inversion. However, since the Zoeppritz equations represent the plane-wave response of a planar interface, it is necessary that the reflectivity estimation also represent the *in situ* plane-wave response of the interface.

From the previous criteria, only the V-stack represents a reasonable approximation to this requirement. To obtain an estimation completely consistent with the plane-wave response it necessary to perform a complete plane-wave decomposition of the upward and downward propagating wavefields at each point of the model, for all

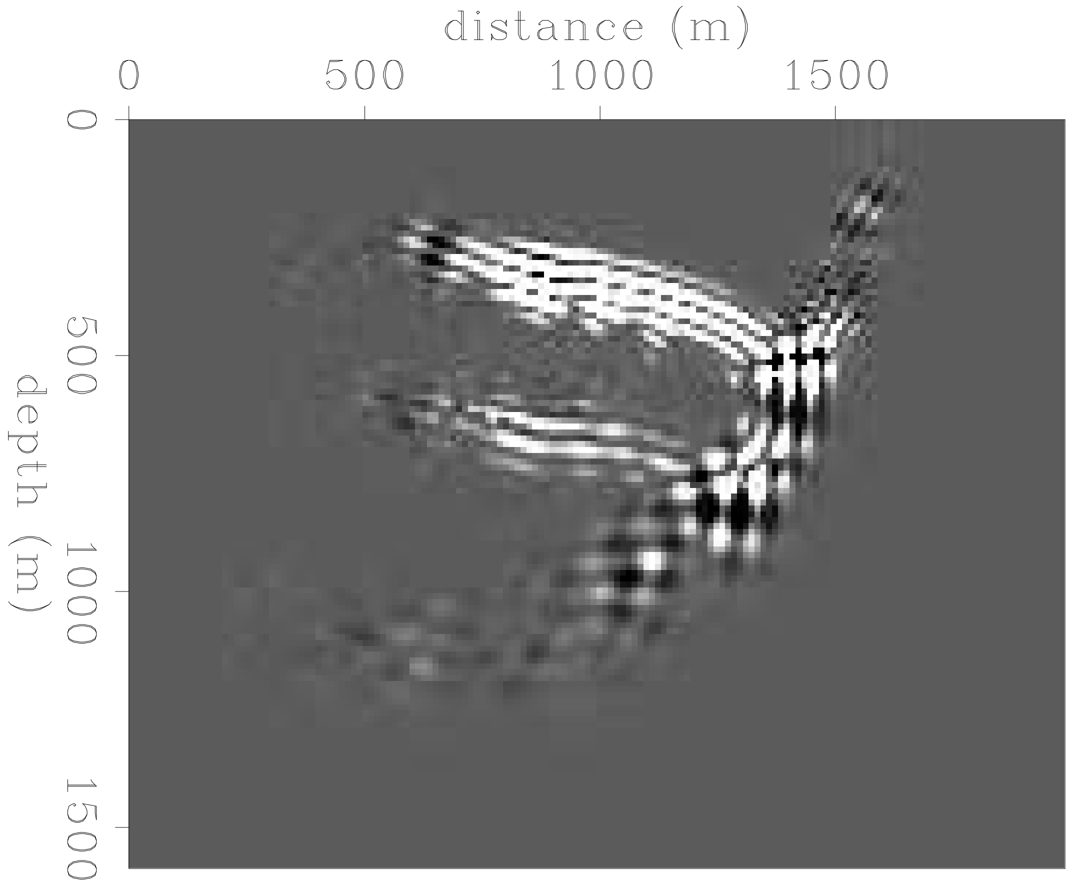

Figure 6: Product of the modeled wavefield ϕ^s and the backward-propagated wavefield ϕ^r for a particular time t when the wavefields intercept two interfaces of the background model. Two V-shaped regions, whose vertex indicate the point of the interface where the wavefield partition takes place, can be observed in the figure carlos3-vshape [NR]

time steps. Although this criterion can be applied to general RTM schemes, it is particularly appropriate for the *one-experiment* approach described in Cunha (1992), where a single wavefield (with combined information form the modeled and recorded wavefields) is backward propagated in time using a discontinuous background model.

The implementation of the plane-wave decomposition criterion for the one-experiment RTM scheme is outlined below

- First, it is necessary to separate the downgoing $\phi^d(x,z,t;x_s)$ and upcoming $\phi^u(x,z,t;x_s)$ components of the wavefield potential, using the propagation-direction unit vector $\hat{\mathbf{k}}(x,z,t;x_s) \;=\; (k_x,k_z)$

$$\begin{aligned} \phi^d(x,z,t;x_s) &= \phi(x,z,t;x_s) && \text{where} \quad k_z < 0 \\ \phi^u(x,z,t;x_s) &= \phi(x,z,t;x_s) && \text{elsewhere.} \end{aligned}$$

  Appendix A describes how to obtain the propagation direction from the field potentials. The downgoing field (within the forward time reference system) includes the incident and the transmitted wavefields, while the upcoming field contains only the reflections[3]. Figure **??** shows the estimated propagation directions overlain on the wavefield and Figure **??** shows the resulting upcoming and downgoing separated wavefields.

- The second step involves the computation of the stacking power of the two wavefields (ϕ^d and ϕ^u) along the directions represented by the angle θ around each point of the model

$$\begin{aligned} \Phi^d(x,z,t,\theta;x_s) &= \int_0^\infty \phi^d(x+l\cos\theta, z+l\sin\theta, t, x_s)\,dl \quad \text{for} \quad 0 \le \theta \le 2\,\pi \\ \Phi^u(x,z,t,\theta;x_s) &= \int_0^\infty \phi^u(x+l\cos\theta, z+l\sin\theta, t, x_s)\,dl. \quad \text{for} \quad 0 \le \theta \le 2\,\pi. \end{aligned}$$

  As in the V-stack case, the stacking power here is computed outward from the image point (stacking trajectories are like a clock's hand), instead of across it. This implies that $\Phi^d(\theta) \neq \Phi^d(\theta+\pi)$. As discussed in appendix B the point of a given interface that intersects the downgoing wavefield at time t (reflection point) will have two directions θ (almost opposite) for which the Φ^d has a local maximum, corresponding to the incident and transmitted waves, but only one direction for which the Φ^u is maximum.

- Evaluate the angle θ^u_{max} for which Φ^u is maximum. For reasons discussed in appendix B this angle determines the subdomain $\Delta\theta(\theta^u_{max})$ in which the correlation between the two stacking power functions is to be evaluated.

- Next, the crosscorrelation $\mathcal{C}$ of the two stacking powers, and the autocorrelation $\mathcal{A}$ of the stacking power of the downgoing wavefield are evaluated, in the interval

[3]Overturning waves are not considered in this analysis

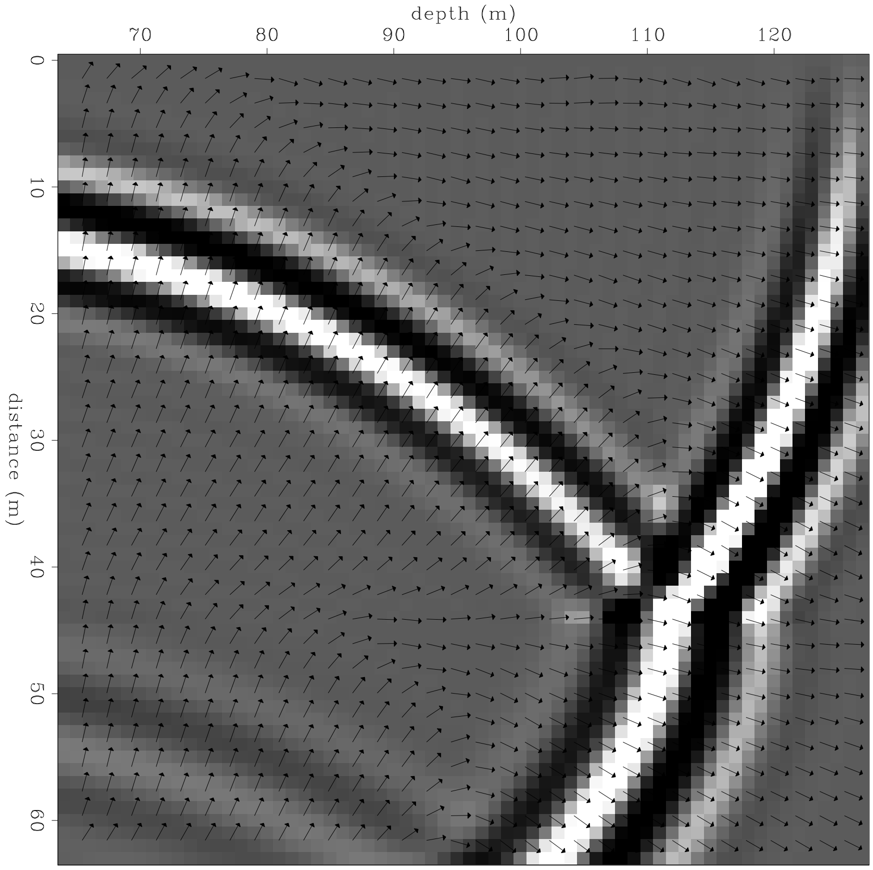

Figure 7: Wavefield partition at an interface. The incident and transmitted wavefields propagate downward while the reflected wavefield propagates upward. The overlaid arrows indicate the local propagation direction estimated from the wavefield as described in appendix A. carlos3-wdir [ER]

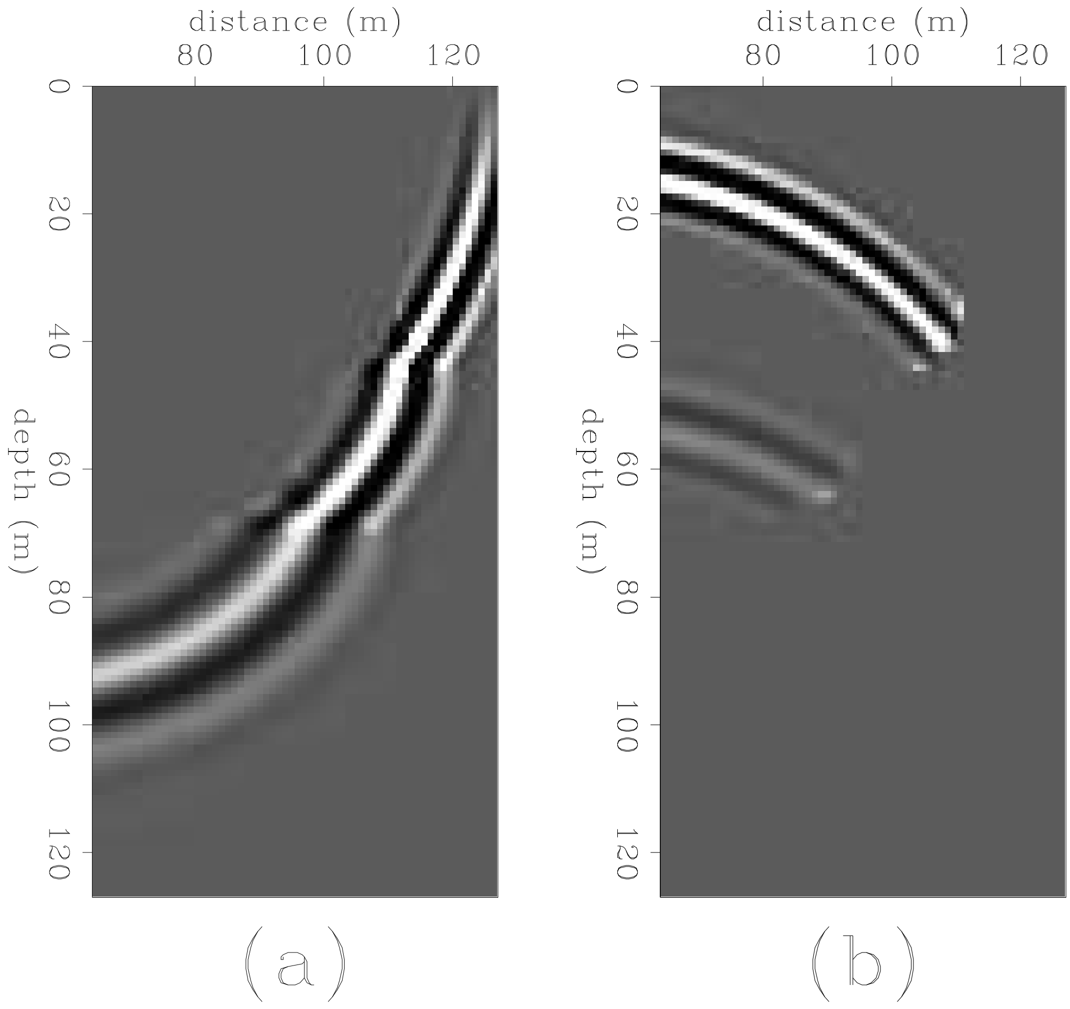

Figure 8: Separation of the upward-propagating and downward-propagating parts of a wavefield using the local propagation direction. (a) The downward-propagating part corresponding to the incident and transmitted wavefields. (b) The upward-propagating part corresponding to the reflected wavefields. carlos3-wavesep [NR]

$\Delta\theta(\theta^u_{max})$

$$\mathcal{C}(x,z,t,\beta;x_s) = \int_{\frac{\pi}{2}}^{\frac{3\pi}{2}} \Phi^u(x,z,t,\theta-\pi+2\beta;x_s)\,\Phi^d(x,z,t,\theta;x_s)\,d\theta$$
$$\mathcal{A}(x,z,t,\beta;x_s) = \int_{\frac{\pi}{2}}^{\frac{3\pi}{2}} \Phi^u(x,z,t,\theta;x_s)\,\Phi^d(x,z,t,\theta;x_s)\,d\theta,$$

for points $(x,z,t;x_s)$ where $-\frac{\pi}{2} \leq \theta^u_{max} \leq \frac{\pi}{2}$, and

$$\mathcal{C}(x,z,t,\beta;x_s) = \int_{-\frac{\pi}{2}}^{\frac{\pi}{2}} \Phi^u(x,z,t,\theta+\pi-2\beta;x_s)\,\Phi^d(x,z,t,\theta;x_s)\,d\theta$$
$$\mathcal{A}(x,z,t,\beta;x_s) = \int_{-\frac{\pi}{2}}^{\frac{\pi}{2}} \Phi^u(x,z,t,\theta;x_s)\,\Phi^d(x,z,t,\theta;x_s)\,d\theta,$$

for points $(x,z,t;x_s)$ where $\frac{\pi}{2} \leq \theta^u_{max} \leq \frac{3\pi}{2}$, where β is the reflection angle.

- The estimated attribute is given by

$$R(x,z,\beta;x_s) = \frac{\int \mathcal{C}(x,z,t,\beta;x_s)\,dt}{E(x,z,\beta;x_s)}, \quad \text{where } E(x,z,\beta;x_s) \geq E_{cut}(x,z,\beta;x_s),$$
$$R(x,z,\beta;x_s) = \frac{\int \mathcal{C}(x,z,t,\beta;x_s)\,dt}{E_{cut}(x,z,\beta;x_s)}, \quad \text{elsewhere}, \tag{12}$$

where

$$E(x,z,\beta;x_s) = \int \mathcal{A}(x,z,t,\beta;x_s)\,dt.$$

Figure **??** shows the twelve images obtained over a small time window centered at the time-frame of Figure **??**. Each of these images correspond to $R(x,z,\beta;x_s)$ at a different local angle of incidence β. The ray-theoretical values for the angle of incidence of the wavefronts that reach the two interfaces at that particular time are: 48 degrees for upper interface and 30.5 degrees for the bottom interface. From the figure it is clear that the point of the upper interface that is imaged at this time has maximum energy at the frames corresponding to 45 and 52.5 degrees, while for the bottom interface the maximum occurs at 30 and 37.5 degrees. Though special care will be required to avoid the undesirable focusing at small angles that we observe in the figure, it is encouraging to see that the location of the main maxima are consistent with the expected values.

SUMMARY

In structurally complex media, the accurate recovery of the angle-dependent reflectivity function requires the use of an elastic prestack migration technique. Mode separation can be done before depth extrapolation or during the imaging step. Though more

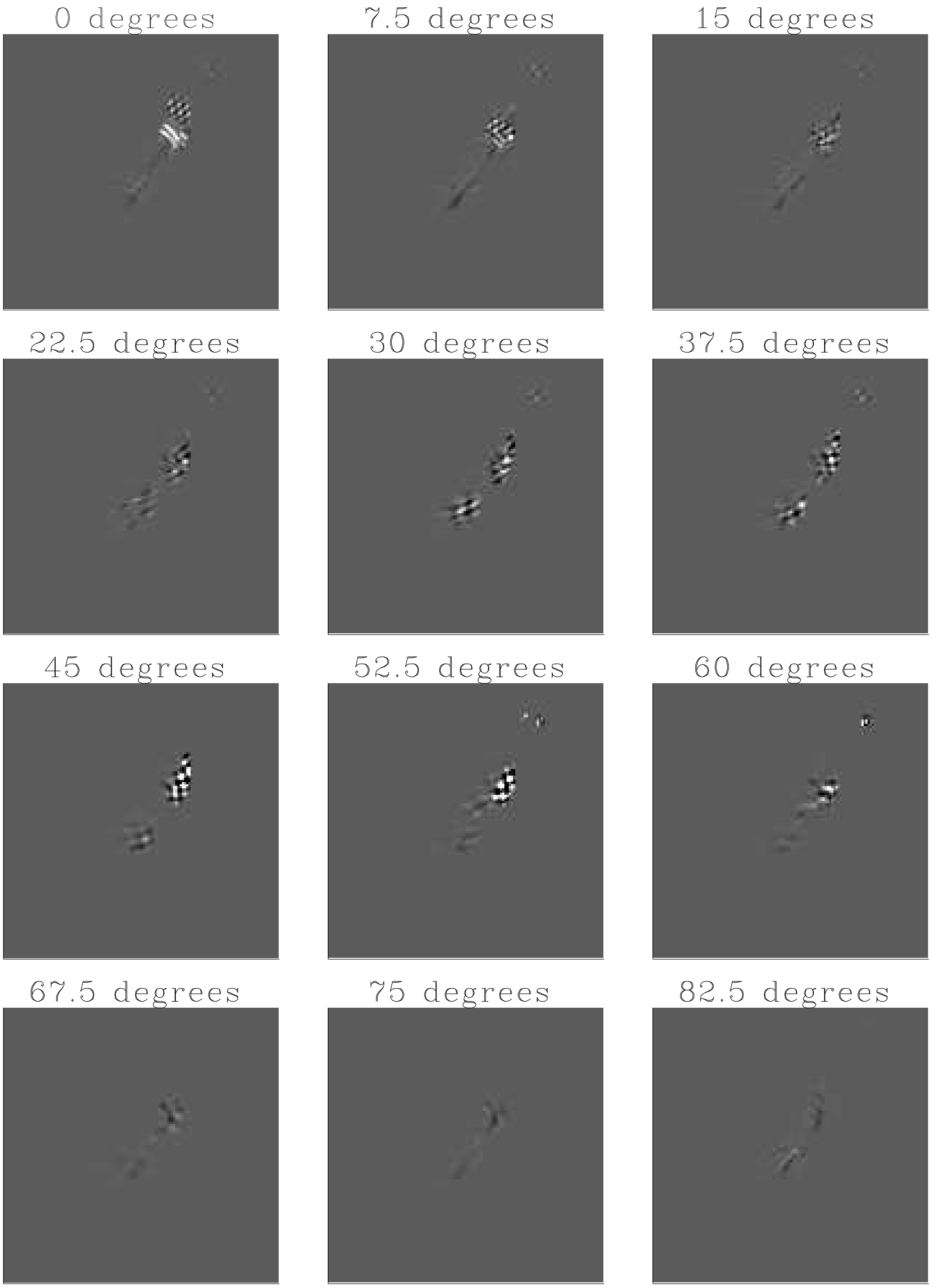

Figure 9: PP reflectivity for a small (6 time steps) time window of the wavefield in Figure **??**, for different values of the angle of incidence β. carlos3-mig1time [NR]

complex, the latter is more complete because it allows the imaging of mode-converted waves. The standard crosscorrelation criterion to implement the imaging condition is not suitable for true reflectivity recovery, especially when imaging reflectivities associated with mode-converted waves. Two new alternative criteria were defined to overcome the limitations of correlation-based imaging conditions. The V-stack criterion accounts for conversion losses of the downgoing wavefield and avoids the imaging of false events associated with an unsmoothed background velocity model. In addition to these advantages, the plane-wave decomposition criterion is designed to generate images that can be directly related to the Zoeppritz equations, since they represent the in-depth plane-wave response of the medium.

ACKNOWLEDGMENTS

I would like to thank David Lumley and Martin Karrenbach for their constructive comments, suggestions and discussions.

REFERENCES

Aki, K., and Richards, P.G., 1980, Quantitative Seismology, vol. I: Freeman and Company.

de Bruin, C.G.M., Wapenaar, C.P.A., and Berkhout, A.J., 1990a: Angle-dependent reflectivity by means of prestack migration: Geophysics, **55**, 1223–1234.

de Bruin, C.G.M., Wapenaar, C.P.A., and Berkhout, A.J., 1990b: Imaging for angle-dependent reflectivity in the presence of dip: 60th Ann. Internat. Mtg., Soc. Expl. Geophys., Expanded Abstracts, 1503–1506.

Chang, W.F., and McMechan, G.A., 1987, Elastic reverse-time migration: Geophysics, **52**, 1365–1375.

Claerbout, J.F., 1971, Toward a unified theory of reflector mapping: Geophysics, **36**, 467–481.

Cunha Filho, C.A., 1990, Snell-beam transform: Retrieving the angle-dependent reflectivity: 60th Ann. Internat. Mtg., Soc. Expl. Geophys., Expanded Abstracts, 1507–1510.

Cunha Filho, C.A., 1992, Elastic inversion of marine data: Ph.D. thesis, Stanford University (in preparation).

Etgen, J.T, 1987, Finite-difference elastic anisotropic wave propagation: SEP–**56**, 23–57.

Hildebrand, S.A., 1987, Reverse-time depth migration: Impedance imaging condition: Geophysics, **52**, 1060–1064.

Jacobs, A., 1982, The pre-stack migration of profiles: Ph.D. thesis, Stanford University.

Karrenbach, M., 1991, Prestack reverse-time migration in anisotropic media: SEP–**70**, 113–121.

Kolb, P., and Chapel, F., 1989, Lithologic inversion: A reflectivity versus angle (RVA) approach: 60th Ann. Internat. Mtg., Soc. Expl. Geophys., Expanded Abstracts, 695–699.

Lumley, D.E., and Beydoun, W.B., 1991, Elastic parameter estimation by Kirchhoff prestack depth migration/inversion: SEP–**70**, 165–192.

Mora, P., 1987, Nonlinear two-dimensional elastic inversion of multioffset seismic data: Geophysics, **52**, 1211–1228.

Newman, P., 1973, Divergence effects in a layered earth: Geophysics, **38**, 481–488.

Tarantola, A., 1986, A strategy for nonlinear elastic inversion of seismic reflection data: Geophysics, **51**, 1893–1903.

Yu, G., 1985, Offset-amplitude variation and controlled-amplitude processing: Geophysics, **50**, 2697–2708.

APPENDIX A

LOCAL SNELL PARAMETER, AND PROPAGATION DIRECTION.

Inversion methods which use the directional dependence of the reflection coefficient to estimate the elastic parameters of the medium (AVO inversion) use in general an angular functionality to express such a dependence. This choice is not always convenient because the angle estimation may be strongly dependent on the macro model that was used in the estimation process. Moreover, the propagation angles are affected by the elastic perturbations that one wishes to estimate, using the angular dependence of the reflectivities. I claim that a more appropriate choice for expressing the directional dependence of the reflection coefficient is the *local Snell parameter*, which is defined as the component of the slowness parallel to the "local reflector plane" at each position of the subsurface. Evidently, not all points of the subsurface can be considered as a reflector, but at all points of interest, where the the upcoming wavefronts intercept the downgoing wavefront, a "reflector plane" can be defined. As defined, the local Snell parameter is conserved for first order perturbations in the local elastic parameters. Although its estimated value will be still dependent on the macro model, it will be much less sensitive to errors in the model than the angle of incidence.

Estimation of the local Snell parameter

Figure **??** shows a descending (incident) wavefield crossing an ascending (reflected) wavefield at a given time step of the backward propagation part of the scheme. The crossing point defines the point of the interface that was imaged at that time, and the angles α and β are measured, respectively, from the tangent and from the normal to the interface at that point.

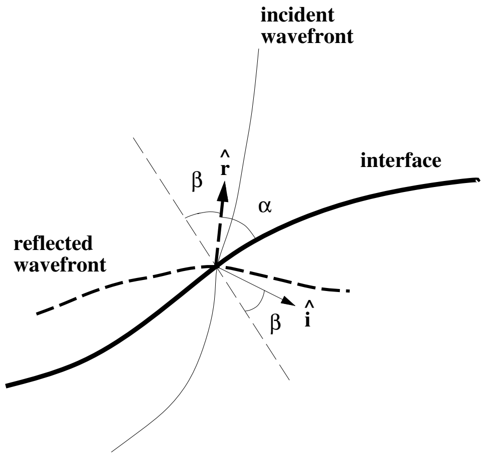

Figure A-1: The points where the ascending and descending wavefronts overlap define the location of the reflector. The reflection angle can be determined by the gradients of the two wavefields at the reflection point, at the time when the reflection occurred. carlos3-reflect [NR]

From the figure we get the following relation,

$$\cos(2\alpha) = \hat{\mathbf{i}} \cdot \hat{\mathbf{r}},$$

where the *unit vectors* $\hat{\mathbf{i}}$ and $\hat{\mathbf{r}}$ represent, respectively, the directions of incidence and reflection. I define the *local Snell parameter* $\tilde{p}$ as the slowness component parallel to the interface at the reflection point

$$\tilde{p} \quad = \quad \frac{\sin(\beta)}{v_p} \quad = \quad \sqrt{\frac{\hat{\mathbf{i}} \cdot \hat{\mathbf{r}} + 1}{2 v_p^2}}, \tag{A-1}$$

where v_p is the P wave group velocity at that particular location. This definition is restricted to an isotropic assumption, but a more general definition can be formulated that includes the anisotropic extension of Snell's law.

Estimation of the propagation direction

The unit vectors $\hat{\mathbf{i}}$ and $\hat{\mathbf{r}}$ are estimated from the potential fields ϕ^s and ϕ^r using the following equations:

$$
\begin{aligned}
\hat{\mathbf{i}} &= -\,\mathrm{signum}(\frac{\partial \phi^s}{\partial t})\frac{\nabla \phi^s}{\mid \nabla \phi^s \mid}, \\
\hat{\mathbf{r}} &= -\,\mathrm{signum}(\frac{\partial \phi^r}{\partial t})\frac{\nabla \phi^r}{\mid \nabla \phi^r \mid}.
\end{aligned}
\tag{A-2}
$$

I demonstrate below that these relations give the correct estimation of the propagation direction for the incident wavefield. Figure **??** shows the wavefield amplitude along the line defined by the gradient of the potential field.

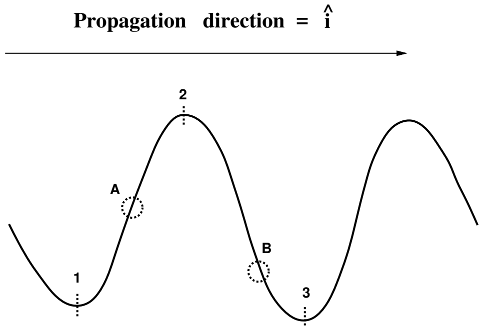

Figure A-2: A representation of the amplitude of potential field along the gradient direction. carlos3-wavedir [NR]

The gradient of the potential field gives the direction, but not the sense of propagation. Any point A in the interval between points 1 and 2 in the figure will have a positive gradient and any point B in the interval between points 2 and 3 will have a negative gradient. Since the propagation direction is positive (to the right) point A will have a negative time derivative, while point B will have a positive time derivative. If the propagation direction was negative (to the left), then the gradients would remain unchanged, while the time derivatives would switch sign. As a result, the product of the gradient and the time derivative at any point will have the opposite sign of the propagation direction.

APPENDIX B

CORRELATION INTERVALS FOR THE PLANE-WAVE DECOMPOSITION

Figure **??** shows a snapshot of a wavefield at the particular time and location where a wavefront is being transmitted/converted, and reflected at an interface. No conversion is observed because only the P wave potential field is displayed. To implement the plane-wave decomposition imaging criterion requires the computation of the slant-stacks around all points in the grid for the upcoming and the downgoing wavefields, at regular angle intervals. These stacks correspond to a semi-plane-wave

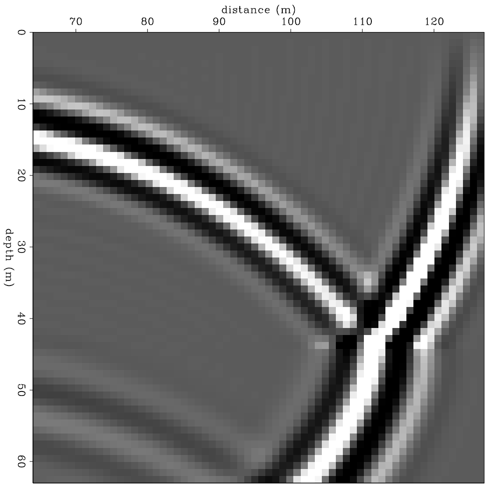

Figure B-1: Snap-shot of a wavefield propagating through an interface. The incident and transmitted wavefronts propagate downward while the reflected wavefront propagates upward. All three wavefronts meet at the point of the interface where the partition takes place at that particular time. carlos3-wavesplit [NR]

decomposition around each point because they are computed from (not across) the grid points.

Lets consider the two functions $\Phi^u(\theta)$ and $\Phi^d(\theta)$, corresponding, respectively, to the stacks of the upcoming and downgoing wavefields around the intersection point of the three wavefronts (incident, transmitted and reflected) in Figure **??**. While $\Phi^u(\theta)$ will have only one maximum, in the direction tangent to the reflected wavefront at that point, $\Phi^d(\theta)$ will have two local maxima; one in the direction tangent to the incident wavefront and one in the direction tangent to the transmitted wavefront. An crucial step in this imaging criterion is the selection of the proper subdomain Θ^i of the distribution $\Phi^d(\theta)$ where the maximum associated with the incident wave is located.

First it is necessary to find the angle θ^u_{max} for which $\Phi^u(\theta)$ is maximum:

$$\Phi^u(\theta^u_{max}) = \max\left[\Phi^u(\theta)\right].$$

As explained below, the location of the subdomain Θ^i, will depend on the quadrant where θ^u_{max} is located.

The following rules are applied in the analysis:

1. The reflected wavefront can only propagate upward and the incident wavefront can only propagate downward.

2. The reflected and incident wavefronts meet the interface at the same angle (Snell law).

3. The reflecting interface is locally planar.

4. The incident wavefront can only propagate towards the interface and the reflected wavefront can only propagate outwards from the interface.

Figure **??** shows four diagrams, each one corresponding to a different quadrant location for θ^u_{max}. The dark bars in each diagram refers to the limit directions of the reflected wavefront (i.e., θ^u_{max}) in each quadrant and the arrows indicate the only possible propagation direction for this wavefront.

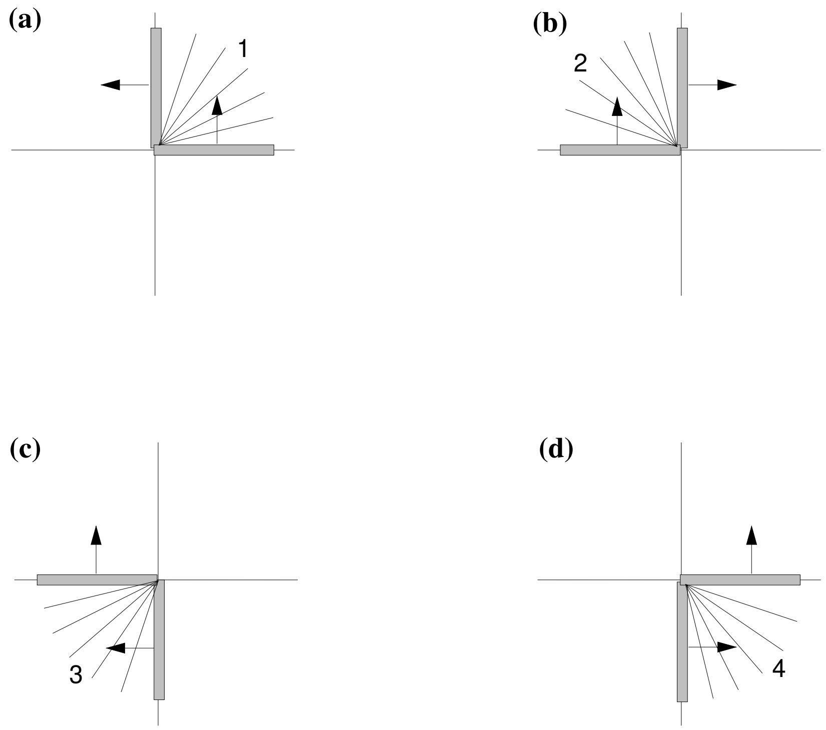

Figure B-2: Diagrams representing the location of the reflected wavefront (dark bars) and its propagation direction (arrows). (a) The reflected wavefront is located in the first quadrant (0–$\pi/2$). (b) The reflected wavefront is located in the second quadrant ($\pi/2$–π). (c) The reflected wavefront is located in the third quadrant (π–$3\pi/2$). (d) The reflected wavefront is located in the fourth quadrant ($3\pi/2$–2π). carlos3-fourquad [NR]

Lets consider each of the four possibilities:

- **a) Reflected wavefront in the first quadrant**
  If the reflected wavefront is horizontal then the incident wavefront must be restricted to the second quadrant, otherwise one of the above stated rules would be violated. If the reflected wavefront is vertical then the incident wavefront must be restricted to the second or third quadrants.

$$0 \le \theta^u_{max} \le \frac{\pi}{2} \quad \longrightarrow \quad \frac{\pi}{2} \le \theta^d \le \frac{3\pi}{2}$$

- **b) Reflected wavefront in the second quadrant**
  If the reflected wavefront is horizontal then the incident wavefront must be

restricted to the first quadrant. If the reflected wavefront is vertical then the incident wavefront must be restricted to the first or fourth quadrants.

$$\frac{\pi}{2} \le \theta^u_{max} \le \pi \quad \longrightarrow \quad -\frac{\pi}{2} \le \theta^d \le \frac{\pi}{2}$$

- **c) Reflected wavefront in the third quadrant**
  If the reflected wavefront is horizontal then the incident wavefront must be restricted to the first quadrant. If the reflected wavefront is vertical then the incident wavefront must be restricted to the first or fourth quadrants.

$$\pi \le \theta^u_{max} \le \frac{3\pi}{2} \quad \longrightarrow \quad -\frac{\pi}{2} \le \theta^d \le \frac{\pi}{2}$$

- **d) Reflected wavefront in the fourth quadrant**
  If the reflected wavefront is horizontal then the incident wavefront must be restricted to the second quadrant. If the reflected wavefront is vertical then the incident wavefront must be restricted to the second or third quadrants.

$$-\frac{\pi}{2} \le \theta^u_{max} \le 0 \quad \longrightarrow \quad \frac{\pi}{2} \le \theta^d \le \frac{3\pi}{2}$$

The above relations can be summarized as

$$-\frac{\pi}{2} \le \theta^u_{max} \le \frac{\pi}{2} \quad \longrightarrow \quad \frac{\pi}{2} \le \theta^d \le \frac{3\pi}{2}$$

$$\frac{\pi}{2} \le \theta^u_{max} \le \frac{3\pi}{2} \quad \longrightarrow \quad -\frac{\pi}{2} \le \theta^d \le \frac{\pi}{2}.$$

Figure **??** is a graphical representation of theses relations. When the reflected wavefront is located in the first or fourth quadrants (dark bar in **??**-a) the incident wavefront must be in the second or third quadrants (white bar). When the reflected wavefront is located in the second or third quadrants (dark bar in **??**-b) the incident wavefront must be in the first or fourth quadrants (white bar). As indicated in the figure the angle between the direction of the two wavefronts is equal to twice the angle of incidence.

Using the above relations, the correlation between the two distributions $\Phi^u(\theta)$ and $\Phi^d(\theta)$ is will be given by

$$\mathcal{C}(\beta) \;=\; \sum_{\theta=\pi/2}^{3\pi/2} \Big[\Phi^u(\theta-\pi+2\beta)\;\Phi^d(\theta)\Big] \qquad \text{if} \quad \frac{-\pi}{2} \le \theta^u_{max} \le \frac{\pi}{2},$$

and

$$\mathcal{C}(\beta) \;=\; \sum_{\theta=-\pi/2}^{\pi/2} \Big[\Phi^u(\theta+\pi-2\beta)\;\Phi^d(\theta)\Big] \qquad \text{if} \quad \frac{\pi}{2} \le \theta^u_{max} \le \frac{3\pi}{2},$$

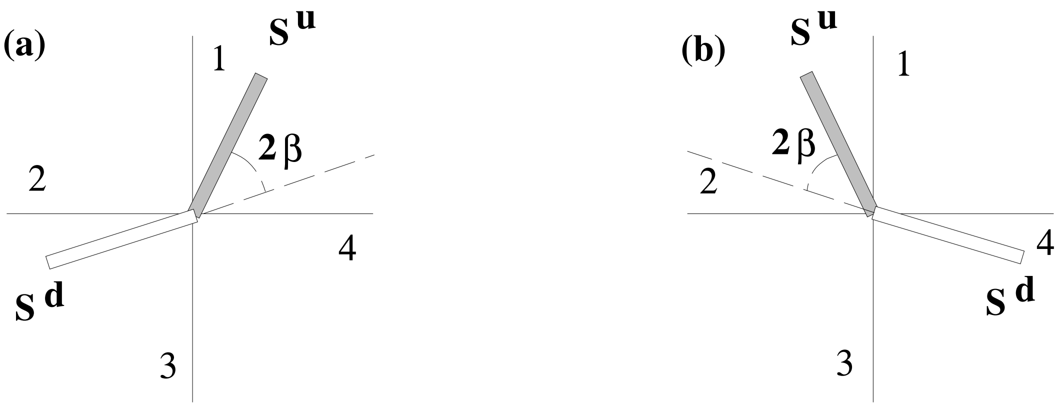

Figure B-3: Diagrams showing the relation between the reflected (dark bar) and transmitted (white bar) wavefronts. (a) If the reflected wavefront is located in the first or fourth quadrants the transmitted wavefront must be located in the second or third quadrants. (b) If the reflected wavefront is located in the second or third quadrants the transmitted wavefront must be located in the first or fourth quadrants. β is the angle of incidence. carlos3-twoquad [NR]

and the autocorrelation of $\Phi^d(\theta)$ by

$$\mathcal{A}(\beta) \;=\; \sum_{\theta=\pi/2}^{3\pi/2} \left[\Phi^d(\theta)\;\Phi^d(\theta)\right] \qquad \text{if} \quad \frac{-\pi}{2} \le \theta^u_{max} \le \frac{\pi}{2},$$

and

$$\mathcal{A}(\beta) \;=\; \sum_{\theta=-\pi/2}^{\pi/2} \left[\Phi^d(\theta)\;\Phi^d(\theta)\right] \qquad \text{if} \quad \frac{\pi}{2} \le \theta^u_{max} \le \frac{3\pi}{2}.$$

The reflectivity estimation for that particular time would be given by the ratio $\mathcal{C}/\mathcal{A}$.